Appl. Magn. Reson. 21, 363–379 (2001)

Applied Magnetic Resonance

High-Frequency EPR Studies on Cofactor Radicals in Photosystem I

C. Teutloff[1], W. Hofbauer[1], S. G. Zech[2], M. Stein[1], R. Bittl[1,2], and W. Lubitz[1,3]

[1] Max-Volmer-Laboratorium, Technische Universität Berlin, Berlin, Germany
[2] Institut für Experimentalphysik, Freie Universität Berlin, Berlin, Germany
[3] Max-Planck-Institut für Strahlenchemie, Mülheim/Ruhr, Germany

Received October 15, 2001

Abstract. Electron paramagnetic resonance (EPR) spectroscopy at W-band (94 GHz) is used to resolve the *g*-tensors of the radical ions of the primary chlorophyll donor $P_{700}^{+\bullet}$ and the quinone acceptor $A_1^{-\bullet}$ in photosystem I. The obtained *g*-tensor principal values are compared with those of the isolated pigment radicals in organic solvents and the shifts are related to an impact of the protein environment. $P_{700}^{+\bullet}$ has been investigated in photosystem I single crystals at 94 GHz. W-band EPR applied to the photoinduced radical pair $P_{700}^{+\bullet}A_1^{-\bullet}$ is used to correctly assign the *g*-tensor axes of $P_{700}^{+\bullet}$ to the molecular structure of the primary donor. Density functional theory calculations on a model of $A_1^{-\bullet}$ in its binding pocket derived from the recent crystal structure of photosystem I were utilized to correlate experimental magnetic resonance parameters with structural elements of the protein.

1 Introduction

Photosystem I (PS I) is a transmembrane protein complex present in oxygenic photosynthetic species like cyanobacteria, algae and green plants. It is composed of at least eleven protein subunits and contains about 100 cofactors. It functions as a light-driven oxidoreductase catalyzing the electron transfer from the lumenal to the stromal side of the membrane. Recently the crystal structure of PS I at a resolution of 0.25 nm was obtained [1]. The arrangement of the cofactors involved in the first steps of the light-induced charge separation process is shown in Fig. 1. After light excitation the primary donor P_{700}, a chlorophyll *a* dimer, donates an electron to an electron transport chain comprising A_0, a chlorophyll *a*, A_1, a phylloquinone (vitamin K_1, VK_1), and subsequently three [4Fe-4S] clusters F_X, F_A and F_B. From the donor a radical cation and from all electron acceptors radical anions are formed that are amenable to electron paramagnetic resonance (EPR) studies. The EPR investigation of the primary donor cation radical

$P_{700}^{+\bullet}$ has recently been described in detail [2]. The structure and function of the quinone acceptor A_1 is, however, less well understood. In PS I it acts as an electron mediator at a very low redox potential compared to the quinones in bacterial reaction centers and PS II [3]. The unusual properties of the phylloquinone in PS I are also reflected in modified magnetic resonance parameters of the radical anion indicating a change of the electronic structure. This is seen from the shifted *g*-tensor principal values [4] and the increase of the methyl hyperfine coupling (hfc) of $A_1^{-\bullet}$ compared with the radical anion $VK_1^{-\bullet}$ in organic solvents [5, 6].

EPR at X-band frequency on chlorophyll and quinone radical ions suffers from limited spectral resolution of the *g*-tensor components which is caused by the substantial hf broadening and the rather small *g*-anisotropy. To overcome this problem, measurements at higher frequencies were performed, where the increased Zeeman interaction leads to a better separation of spectral features [7]. First EPR investigations on $VK_1^{-\bullet}$ at Q-band date back to Hales et al. [8] and gave some information about the *g*-tensor and hfcs. Burghaus et al. [9] performed EPR investigations at W-band (95 GHz) on a series of quinone radical anions in proto-

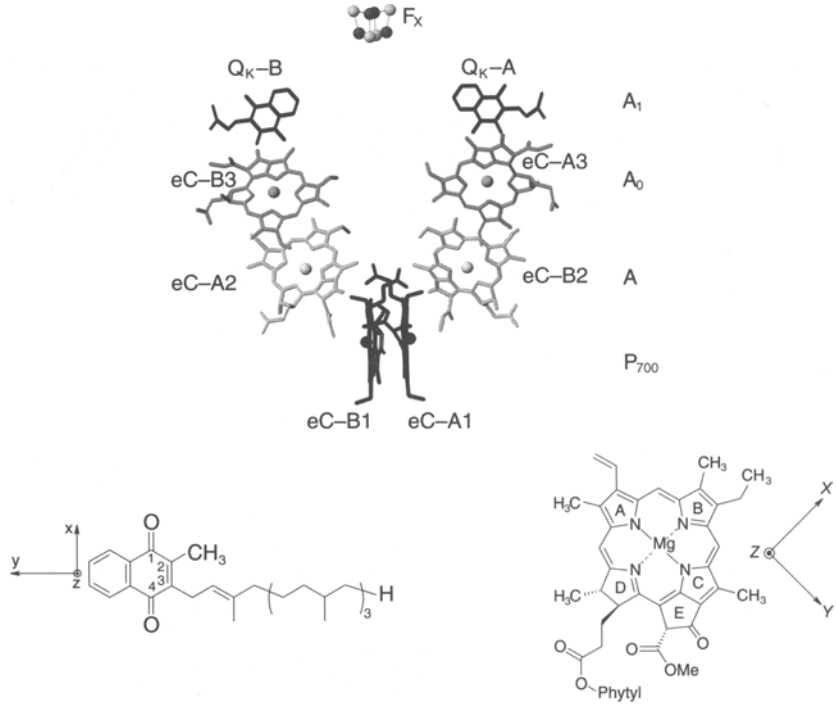

Fig. 1. Top: arrangement of the cofactors in PS I obtained from the X-ray structure analysis [1]. The final acceptors F_A and F_B are omitted here. The phytyl chains of all cofactors are truncated for clarity. Bottom: molecular structure of vitamin K_1 (left) and chlorophyll *a* (right) with their molecular axes systems.

nated and deuterated organic solvents, including $VK_1^{-\bullet}$, and demonstrated the better resolution of the *g*-tensors. The observed *g*-tensor shifts between protic and aprotic solvents were related to the presence or absence of hydrogen bonds to the quinone oxygens [9]. High-field EPR experiments on the photoaccumulated radical $A_1^{-\bullet}$ in PS I at 283 GHz [10] and 94 GHz [11] revealed the *g*-tensor of the phylloquinone anion radical in vivo. A final interpretation of the *g*-value shifts observed for this radical in vitro and in the protein is, however, still lacking.

The increased Zeeman resolution at W-band is also obvious in transient (TR) EPR spectra of the light-induced radical pair (RP) $P_{700}^{+\bullet}A_1^{-\bullet}$ [4]. The TR spin-polarized spectra of such RPs provide a sensitive probe for structural parameters of the two cofactors involved. Consequently, TR and pulsed EPR spectroscopy on these RPs are useful complements to crystallographic studies [12–14]. However, a clear interpretation of the spectra can only be achieved if some of the parameters entering the numerical simulations of the RP spectra can be provided by independent experiments. Since the number of magnetic parameters, such as *g*-values and hfc constants, determined independently increased considerably for the cofactors in PS I through the last years, TR-EPR of $P_{700}^{+\bullet}A_1^{-\bullet}$ can now be used to remove some remaining ambiguities which could not be settled by other experimental techniques.

In this paper we review the determination of the *g*-tensor principal values of $A_1^{-\bullet}$ and $P_{700}^{+\bullet}$ in PS I and compare the data with some new results derived from the respective model systems in vitro. From high-field EPR experiments of $P_{700}^{+\bullet}$ in PS I single crystals and of $P_{700}^{+\bullet}A_1^{-\bullet}$ in frozen solution the full orientation of the *g*-tensor axes for $P_{700}^{+\bullet}$ is obtained. By density functional theory (DFT) calculations performed on $A_1^{-\bullet}$ in the protein pocket a possible explanation of the unusual EPR parameters of this species is provided. Furthermore, a relationship between the functional properties of A_1 in PS I and its electronic structure is discussed.

2 Materials and Methods

The continuous-wave (cw) EPR experiments at X-band were carried out on a Bruker ESP300 spectrometer equipped with an ER4102ST (TE_{102} rectangular cavity) and an Oxford ESR910 liquid helium cryostat with Oxford ITC4 temperature control unit. Q-band spectra were recorded on the same spectrometer with a Bruker ER051QG microwave bridge and an ER5106QT resonator. EPR measurements at W-band were performed with a Bruker Elexsys E680 spectrometer with an Oxford CF935 helium cryostat. The magnetic field was calibrated at all frequencies against a Li:LiF sample ($g = 2.002293$) [15].

The preparation of PS I particles and the crystallization of PS I from the cyanobacterium *Synechococcus elongatus* is described in ref. 16. The mounting of the PS I single crystals followed a procedure described elsewhere [17]. Generation of the radical cation $P_{700}^{+\bullet}$ was achieved by illumination of the frozen samples in the cavity or by freezing the samples in liquid nitrogen under illumi-

nation. The light-induced RP $P_{700}^{+\bullet}A_1^{-\bullet}$ has been generated by in situ repetitive laser irradiation in the W-band cavity via a quartz fiber as described in ref. 17. For the generation of the radical anion $A_1^{-\bullet}$ in PS I a photoaccumulation procedure was used as outlined in ref. 10. PS I particles were prereduced in the dark for 30 min with 30 mM dithionite in 200 mM glycine buffer at pH 10. The $A_1^{-\bullet}$ radical anion was then photoaccumulated by illumination with white light (150 W halogen lamp) filtered through a water filter for 5 min at 205 K.

VK_1 was purchased from Merck (98%) and used without further purification. The radical anion in isopropanol (IP) was generated with a 10 mM quinone solution and a tenfold excess of potassium tert-butylate as a base [18]. In the ether (mixture of 66% 1,2-dimethoxyethane [DME] and 3% 2-methyltetrahydrofurane [MTHF]) the radical was produced electrochemically via cathodic reduction of a 3 mM quinone solution with a tenfold excess of tetra n-butyl ammonium tetrafluoroborate as supporting electrolyte. These samples were prepared on a vacuum line and sealed under vacuum after several freeze-pump-thaw cycles [18].

The efficiently parallelized DFT code DGauss [19] (BP86/DZVP exchange correlation functional and basis set) was employed for geometry optimizations of the radical anion $A_1^{-\bullet}$ in its protein pocket. There were no drastic structural reorientations of the amino acids during the optimization. The *g*-tensor calculations were performed on the optimized model with the two-component relativistic ZORA Hamiltonian in the ADF program [20]. HFCs were calculated with the B3LYP hybrid functional and the EPR II basis set in the Gaussian 98 program [21].

3 Results and Discussion

3.1 Experiments on $P_{700}^{+\bullet}$ in PS I

The EPR spectrum of $P_{700}^{+\bullet}$ in frozen solution shows even at W-band no *g*-tensor resolution. Obviously, the *g*-anisotropy is very small and the inhomogeneous linewidth quite large. However, the spectra obtained for $P_{700}^{+\bullet}$ in PS I single crystals exhibit some resolved features depending on the crystal rotation angle. Such orientation-dependent spectra are shown in Fig. 2. One crystal (Fig. 2, left) was mounted with the *c*-axis parallel to the rotation axis. For the other set of spectra (Fig. 2, right) the crystallographic *c*-axis was in the plane of the magnetic field, perpendicular to the rotation axis. The orientation-dependent effective *g*-values for the six inequivalent sites in the crystal ($P6_3$ space group) are indicated by solid lines. For reference, spectra of $P_{700}^{+\bullet}$ in frozen solution are also shown (Fig. 2, top).

The partially resolved features can be used to fit the orientation dependence as indicated in Fig. 2 (see also ref. 17). Since the individual EPR lines are not fully resolved, the fitting procedure was based on simulations of the orientation-dependent spectra. Taking the $P6_3$ symmetry into account, each set of spectra is

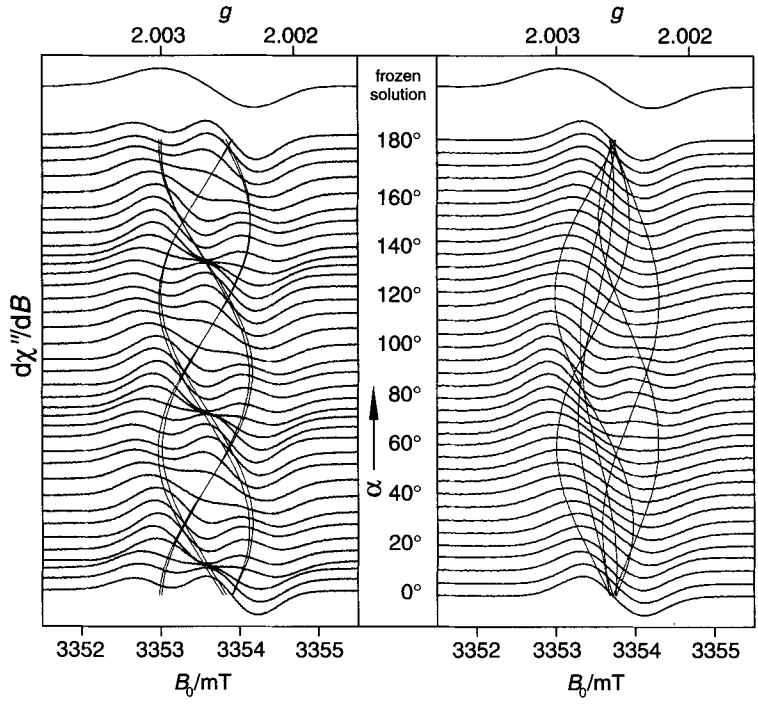

Fig. 2. Frozen solution (top) and orientation-dependent single-crystal spectra of $P_{700}^{+\bullet}$ in PS I at 80 K. Left: rotation around the crystallographic *c*-axis. Right: rotation axis perpendicular to the *c*-axis. The effective *g*-values of the six sites in the crystal are indicated by solid lines. For experimental conditions see ref. 17.

characterized by 10 parameters (3 principal values of the *g*-tensor, 6 Euler angles for the orientation of the *g*-tensor in the crystallographic reference frame together with the orientation of the crystal in the laboratory frame, and one Gaussian linewidth parameter). Since the crystallographic *a*- and *b*-axes are not unique axes in the EPR experiments, one of the six Euler angles cannot be determined from a fit of the EPR spectra alone. Thus, additional X-ray diffraction experiments were performed (not shown). With this information the complete orientation of the $P_{700}^{+\bullet}$ *g*-tensor in the crystal could be obtained. However, a sixfold ambiguity still remains due to the six inequivalent PS I units in the crystal. This problem is solved by additional experiments on the RP $P_{700}^{+\bullet}A_1^{-\bullet}$ (see below). The $P_{700}^{+\bullet}$ *g*-tensor principal values obtained from the single-crystal experiments are in good agreement with results obtained in other works (see Table 1). Deuterated samples [22] and/or significantly higher microwave frequencies [7, 23] were required to obtain the *g*-tensor from experiments on disordered samples. The principal *g*-values of $P_{700}^{+\bullet}$ are quite similar to those of monomeric Chl $a^{+\bullet}$ in organic solvents (Table 1).

Table 1. *g*-Tensor principal values of the radicals $P_{700}^{+\bullet}$ and $A_1^{-\bullet}$ and the respective models Chl $a^{+\bullet}$ and $VK_1^{-\bullet}$ obtained from high-frequency EPR experiments. The experimental error is $5 \cdot 10^{-4}$.

Radical[a]	g_x	g_y	g_z	Reference or source	ν_{mw}(GHz)
$P_{700}^{+\bullet}$ (PS I)	2.00309	2.00260	2.00223	17, this work	94
$P_{700}^{+\bullet}$ (PS I)[b]	2.00317	2.00264	2.00226	23	325
$P_{700}^{+\bullet}$ (PS I)[c]	2.00307	2.00260	2.00226	23	325
$P_{700}^{+\bullet}$ (PS I)[d]	2.00304	2.00262	2.00232	22	140
Chl $a^{+\bullet}$ (MCl)[d]	2.00329	2.00275	2.00220	7	330
$VK_1^{-\bullet}$ (IP)	2.00578	2.00503	2.00224	this work	94
$VK_1^{-\bullet}$ (D-M)	2.00623	2.00505	2.00220	this work	94
$VK_1^{-\bullet}$ (IP)	2.00579	2.00498	2.00218	9	95
$A_1^{-\bullet}$ (PS I)	2.00625	2.00512	2.00220	this work	94
$A_1^{-\bullet}$ (PS I)[c]	2.0062	2.0051	2.0022	17	94
$A_1^{-\bullet}$ (PS I)	2.00625	2.00503	2.00227	10	283

[a] Solvents used for the model systems $VK_1^{-\bullet}$ (IP, isopropanol; D-M, DME-MTHF) and Chl $a^{+\bullet}$ (MCl, methylene chloride).
[b] 40 K.
[c] 200 K.
[d] Deuterated sample.
[e] Determined from the RP $P_{700}^{+\bullet}A_1^{-\bullet}$.

3.2 The Radical Pair $P^{!\bullet}_{700}A_1^{\#\bullet}$

In situ illumination of PS I particles at 80 K generates the RP $P_{700}^{+\bullet}A_1^{-\bullet}$, which can be observed by TR-EPR in various frequency bands [12]. An experiment performed on fully deuterated PS I at W-band is shown in Fig. 3 (dotted trace) (see also ref. 17). In this spin-polarized spectrum the correlated subspectra of $A_1^{-\bullet}$ with g_x^Q, g_y^Q, g_z^Q and $P_{700}^{+\bullet}$ with g_x^P, g_y^P, g_z^P are quite well resolved.

With the *g*-tensor orientation determined by W-band cw-EPR on PS I single crystals (see above), six orientations of $g(P_{700}^{+\bullet})$ with respect to the molecular axes are possible. Neither cw-EPR alone nor additional X-ray crystallographic assignments of the crystallographic-axes can, in principle, deliver sufficient information to remove this sixfold ambiguity. Hence, additional information is required which is provided by TR-EPR experiments of the RP state which can finally yield the correct assignment of the *g*-tensor axes orientations.

Figure 3 shows numerical simulations of the RP state $P_{700}^{+\bullet}A_1^{-\bullet}$ for all six possible orientations of the *g*-tensor of $P_{700}^{+\bullet}$. For the simulations, the orientation of the *g*-tensor in $A_1^{-\bullet}$ ($g_x(A_1^{-\bullet})$ is along the C-O axes, $g_z(A_1^{-\bullet})$ is parallel to the ring normal) and of the $P_{700}^{+\bullet}$-$A_1^{-\bullet}$ dipolar axis, z_D, with Q_K-A, and eC-B1, see Fig. 1, have been calculated from the X-ray structure [1]. The choice of Q_K-A and eC-B1 for the constituents of the RP state $P_{700}^{+\bullet}A_1^{-\bullet}$ is based on experiments with site-directed mutants of PS I showing that the unpaired spin density in $P_{700}^{+\bullet}$ is almost exclusively located on eC-B1 [24, 25] and the EPR-active phylloquinone is Q_K-A [26]. The reference system ($g(A_1^{-\bullet})$) and the Cartesian (**a**, **a** × **c**, **c**) crystal axes frame (CF) (Table 2) are related by the Euler

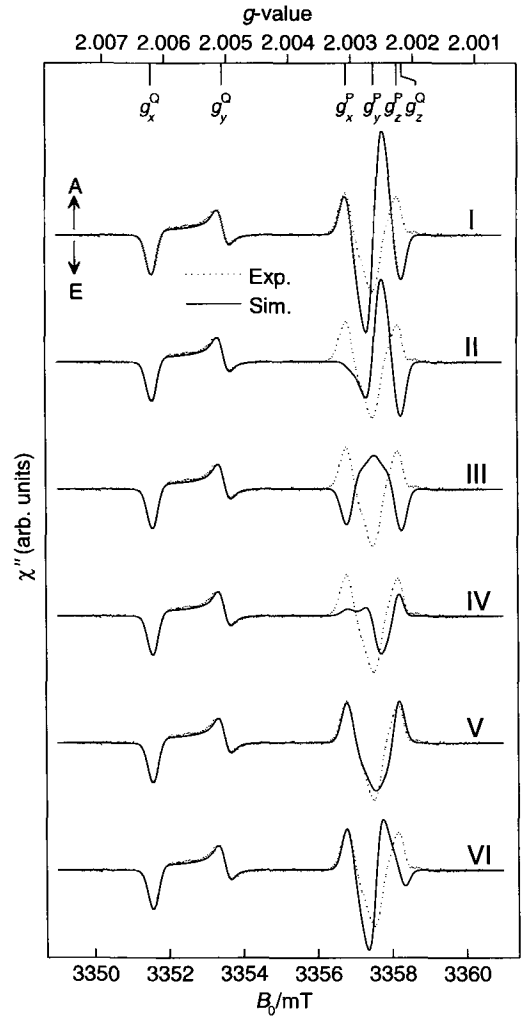

Fig. 3. Dependence of the calculated TR-EPR spectrum of $P_{700}^{+\bullet}A_1^{-\bullet}$ at W-band on the rotation of the $g(P_{700}^{+\bullet})$-tensor about the crystallographic c-axis in steps of 60° (traces I to VI). For comparison the experimental spectrum [17] is also shown (dotted line).

angles $\alpha_{CF} = 241°$, $\beta_{CF} = 112°$ and $\gamma_{CF} = 150°$. The dipolar axis z_D is defined by $\theta_D = 101°$ and $\phi_D = 177°$. The g-values were determined by independent EPR methods (see Table 1). The g-tensor orientation of $P_{700}^{+\bullet}$ with respect to the crystal axes system as given in Table 2 has been used. The six possible remaining orientations of $g(P_{700}^{+\bullet})$ with respect to its molecular axes system are related to each other by a 60° rotation of the tensor axes about the c-axis.

Since these six orientations for $g(P_{700}^{+\bullet})$ differ significantly in the angles between the g-tensor axes and the axis of the dipolar coupling, z_D, the simulated

Table 2. $P_{700}^{+\bullet}$ *g*-tensor orientation (x_P, y_P, z_P,) in single crystals of PS I from *Synechococcus elongatus* relative to a Cartesian frame spanned by the crystallographic *a*-, *c*-axes and a direction perpendicular to *a* and *c* (left) and to the molecular axes system (X_{Chl}, Y_{Chl}, Z_{Chl}) of the Chl *a* molecule P_B (eC-B1), see Figs. 1 and 5. Error 5°.

	x_P	y_P	z_P		x_P	y_P	z_P
a	25°	114°	91°	X_{Chl}	120°	30°	88°
c × **a**	79°	63°	151°	Y_{Chl}	139°	115°	120°
c	68°	38°	61°	Z_{Chl}	114°	106°	30°

TR-EPR spectra of $P_{700}^{+\bullet}A_1^{-\bullet}$ in frozen solution of deuterated PS I show a strong sensitivity on the $g(P_{700}^{+\bullet})$ orientation. As obvious from Fig. 3, the best agreement with the experimental spectrum is found for V, whereas all other orientations show a poor agreement with the experiment. For orientation V, the Euler angles which relate the $g(P_{700}^{+\bullet})$ tensor and the reference system ($g(A_1^{-\bullet})$) are $\alpha_P = 174°$, $\beta_P = 100°$ and $\gamma_P = 213°$. The angles between the *g*-tensor axes of $A_1^{-\bullet}$ and $P_{700}^{+\bullet}$ with respect to the dipolar coupling axis z_D (connecting $A_1^{-\bullet}$ and $P_{700}^{+\bullet}$) are collected in Table 3.

Figure 4 compares the TR-EPR spectra of $P_{700}^{+\bullet}A_1^{-\bullet}$ at W-band simulated with parameters obtained from other spectroscopic methods. The top trace in Fig. 4 is identical to orientation V in Fig. 3 as determined in this study. In Fig. 4, middle trace, the calculated spectrum obtained from a fit of the experimental $P_{700}^{+\bullet}A_1^{-\bullet}$ spectrum as published earlier [17] is shown. The precise tensor orientation obtained in this work on the basis of single-crystal experiments corroborates our previously published data within their larger error margins (Table 3). The spectrum simulated with parameters obtained from the analysis of zero quantum beats in Q-band in combination with partially oriented whole cells measured at W-band [27] shows a less good agreement with the experimental spectrum, especially in the $P_{700}^{+\bullet}$ (high-field) region of the spectrum.

Table 3. Orientation of the dipolar axis, z_D, and the membrane normal, **n**, with respect to the principal axes of $g(Q^{\bullet-})$ and $g(P^{\bullet+})$.

$\angle(z_D, g(Q^{\bullet-}))$			$\angle(z_D, g(P^{\bullet+}))$			$\angle(n, g(Q^{\bullet-}))$			$\angle(n, g(P^{\bullet+}))$			Reference
x_Q	y_Q	z_Q	x_P	y_P	z_P	x_Q	y_Q	z_Q	x_P	y_P	z_P	or source
11°	87°	79°	84°	55°	35°	36°	63°	68°	68°	38°	61°	this work[a]
0°	90°	90°	83°	55°	36°	27°	79°	65°	69°	36°	62°	17[b]
20°	74°	78°	72°	45°	51°	23°	83°	68°	48°	44°	81°	27

[a] The *g*-tensor of $A_1^{-\bullet}$ is assumed to be collinear with the molecular axes system of Q_K-A in the X-ray structure. The angles for the *g*-tensor of $P_{700}^{+\bullet}$ as determined by EPR spectroscopy correspond to orientation V in Fig. 3. Error 5°.

[b] Obtained from the fit of TR-EPR spectra of $P_{700}^{+\bullet}A_1^{-\bullet}$. Error 10°.

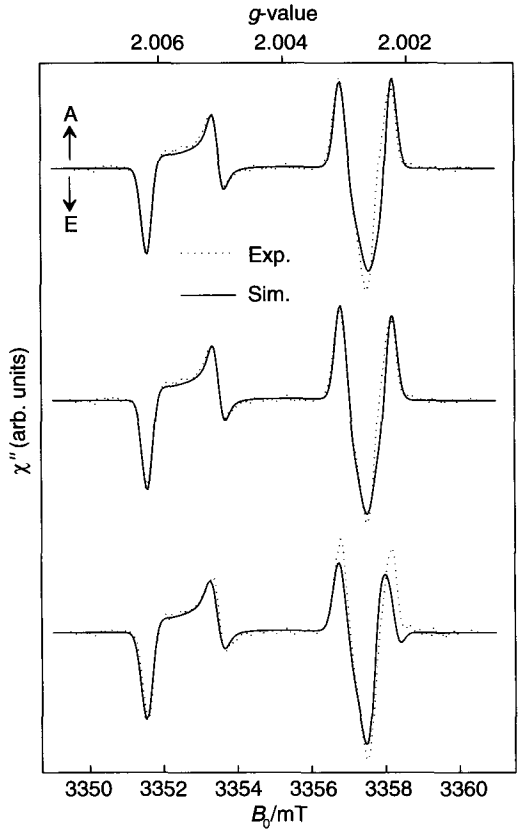

Fig. 4. Comparison of the calculated TR-EPR spectra with structural parameters obtained by various methods. Top: this work. The g-tensor of $A_1^{-\bullet}$ is assumed to be collinear with the molecular axes frame of the Q_K-A quinone [1]. The orientation of the tensor of $P_{700}^{+\bullet}$ corresponds to option V in Fig. 3. Middle: orientation of the tensor axes as obtained in ref. 17 from a fit of TR-EPR spectra of $P_{700}^{+\bullet}A_1^{-\bullet}$ of deuterated PS I in single crystals. Bottom: tensor orientation obtained from a fit of TR-EPR spectra of partially oriented whole cells in combination with an analysis of quantum beat oscillations [27]. The experimental spectrum is shown as dotted line.

Figure 5 depicts the orientation of the g-tensor axes system in the molecular axes frame of the spin-carrying Chl *a* molecule (P_B) [24] constituting $P_{700}^{+\bullet}$. It can be seen that the tensor axes clearly deviate from the molecular axes system. This was also found in previous studies performed on bRC [28, 29] and PS I [17, 27]. The angles between the molecular axes of the spin-carrying Chl *a* molecule and the g-tensor axes of $P_{700}^{+\bullet}$ are given in Table 2. Here, X_{Chl} and Y_{Chl} are defined to be parallel to the N_B-N_D and the N_C-N_A axes of Chl *a*, respectively, whereas the Z_{Chl} axis is the normal to the (average) Chl *a* plane, see Fig. 1.

Inspection of Table 2 reveals a deviation of the z_P-axis of $g(P_{700}^{+\bullet})$ from the molecular Z_{Chl}-axis by 30°. Such a large deviation is unusual for a planar π-system, where the z-axis of the g-tensor is expected to be almost parallel to the

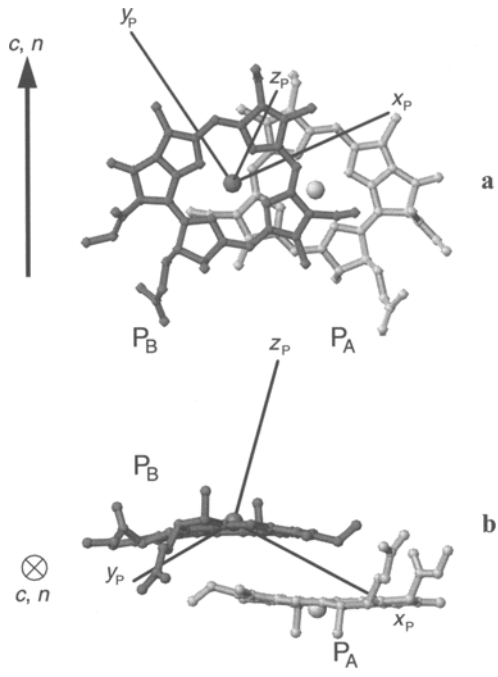

Fig. 5. Orientation of the axes of $g(P_{700}^{+\cdot})$ within the molecular frame of the primary donor Chl *a* molecule P_B (eC-B1, see Fig. 1). **a** View direction parallel to the molecular *z*-axis of P_B and perpendicular to the crystallographic *c*-axis. **b** View parallel to the *c*-axis.

molecular Z_{Chl}-axis. The reason for such a significant difference is not fully understood at present. Possible explanations involve (i) a special geometry of the chlorophyll carrying the spin, (ii) a specific interaction with the surrounding amino acids and (iii) interactions with other pigments, e.g., the other Chl *a* (P_A, eC-A1 in Fig. 1), which is actually a Chl *a'* [1], or other chlorophylls of the ET chain.

3.3 Experiments on $A_1^{-\cdot}$ in PS I and Vitamin $K_1^{-\cdot}$ In Vitro

EPR spectra of $A_1^{-\cdot}$ obtained at X-, Q- and W-band frequencies are shown in Fig. 6. At X-band a large hyperfine quartet dominates the spectrum, which is characteristic for the photoaccumulated $A_1^{-\cdot}$ in cyanobacterial PS I [10] (see Fig. 6, bottom). This hfc is attributed to the methyl group attached to the quinone at position 2 (Fig. 1) [5, 6]. At 34 GHz the *g*-anisotropy becomes dominant as compared to the hf interaction and g_x, g_y and g_z can be obtained (Fig. 6, center). At W-band the increased Zeeman resolution leads to a full resolution of all three *g*-tensor components (Fig. 6, top). In order to get accurate *g*-values, the EPR spectra were simulated (Fig. 6, dashed lines). The methyl proton hf tensor components which were obtained independently from ENDOR spectroscopy [6]

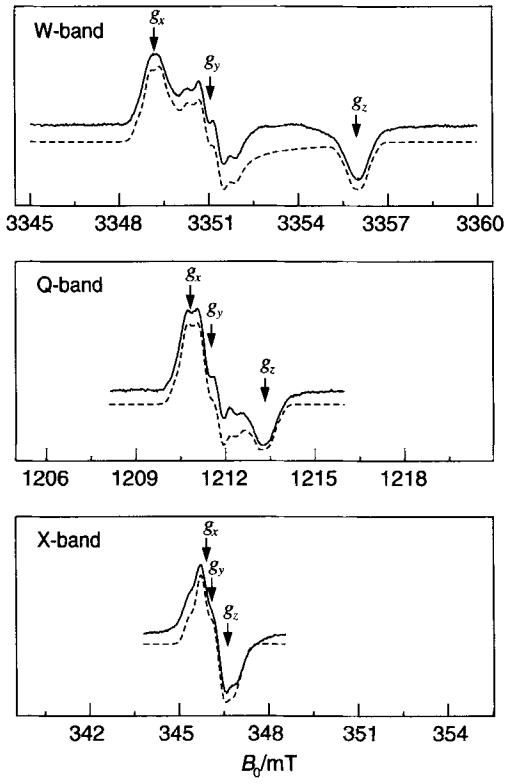

Fig. 6. EPR spectrum of the photoaccumulated radical anion $A_1^{-\bullet}$ at W-band (94.0 GHz), Q-band (34.0 GHz) and X-band (9.7 GHz). The dashed lines indicate simulations. For g- and hf-tensor values used see Table 1 and text. Experimental conditions: $T = 80$ K; nonsaturating microwave power; field modulation depth, 0.1 mT.

were used as input parameters ($A_{||} = 12.8$ MHz, $A_{\perp} = 9.0$ MHz). The other hfcs are small and were subsumed in the linewidth (0.4 mT). A simulation of the spectra at all three frequencies gave accurate g-tensor principal values and the orientation of the methyl proton hfc tensor with respect to the g-tensor ($\angle A_{||}$-$g_y = 30°$, in plane). A summary of the obtained g-values and a comparison with data from the literature is shown in Table 1.

In order to determine the effect of the protein environment on the g- and methyl proton hf-tensors, EPR spectra of $VK_1^{-\bullet}$ in frozen organic solvents were recorded. As a polar protic solvent isopropanol (IP) was chosen which is known to form strong hydrogen bonds with quinones [8]. The ethers DME and MTHF were used as an apolar nonprotic solvent mixture. The spectra of $VK_1^{-\bullet}$ in these two environments are shown in Fig. 7. There is no resolved hyperfine structure indicating a significantly reduced methyl hfc in both samples. Furthermore, the g-tensors are different in these solvents, which is particularly pronounced for the g_x component (see Table 1).

The large differences in the g-values of $VK_1^{-\bullet}$ in IP and DME-MTHF is a consequence of the different solvent properties, i.e., polarity and formation of specific hydrogen bonds. The aprotic and apolar DME-MTHF leads to the upshift of g_x due to the absence of hydrogen bonds. This can be understood in the frame of the g-tensor theory of Stone [30], which relates the g-shift $\Delta g_x \propto \rho_O^{\pi} \xi_O / \Delta E_{n\pi^*}$ to the oxygen spin density ρ_O^{π}, the spin-orbit coupling constant ξ_O and the energy gap $\Delta E_{n\pi^*}$ between the nonbonding (n) and the antibonding (π^*) orbital. Hydrogen bonds lead to a reduced spin density at the carbonyl oxygens and to an increased energy gap caused by stabilization of the n-orbital and therefore to a decrease of g_x [9, 11].

An interesting point is that the g-tensor of $VK_1^{-\bullet}$ in DME-MTHF is within error the same as that of $A_1^{-\bullet}$ in the protein. This indicates that A_1 is located in a hydrophobic environment comparable to an ether solvent shell. However, a comparison of the methyl hfcs shows a remarkable increase from $VK_1^{-\bullet}$ in vitro (a_{iso} = 7.3 MHz) to $A_1^{-\bullet}$ in vivo (a_{iso} = 10.3 MHz). This indicates a changed spin density distribution in the quinone ring which can be attributed to an asymmetric hydrogen bond to the oxygen O-4 adjacent to the phytyl chain (Fig. 1), for a discussion see ref. 31. Such an H-bond has also been confirmed by the X-ray

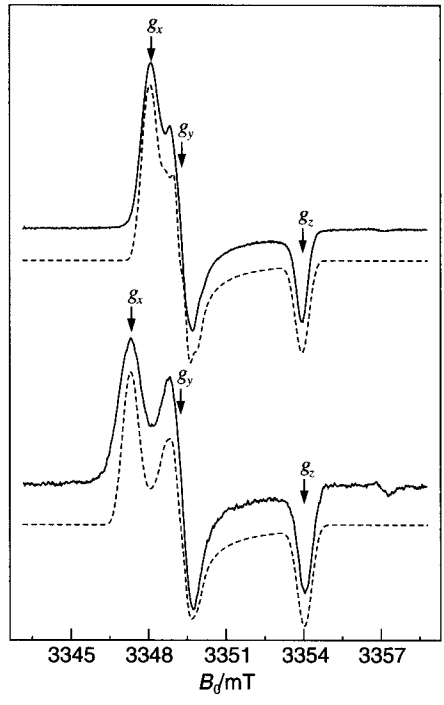

Fig. 7. W-band EPR spectrum of $VK_1^{-\bullet}$ in IP (top) and DME-MTHF (bottom); remarkable is the shift of g_x comparing the radical in protic and aprotic solvents. Experimental conditions: T = 80 K; ν_{mw} = 93.9626 GHz; microwave power, 0.16 μW; field modulation depth, 0.1 mT.

structure at 0.25 nm resolution [1]. Obviously, this single H-bond from the protein affects the g-tensor of $A_1^{-\bullet}$ to a lesser extent than the H-bonds affect $g(VK_1^{-\bullet})$ in a protic solvent. Semiempirical [32] and DFT calculations [33] of the g-tensor of semiquinone radicals have shown that at least four H-bonding solvent molecules are necessary to get satisfying agreement with experimental values. This effect is further analyzed here by DFT calculations (see below).

3.4 DFT Calculations

In order to relate the observed g- and hf-tensor components and their changes to the structure of $A_1^{-\bullet}$ in its binding site, DFT calculations were performed. For the electronic structure calculations, the quinone A_1 cofactor and its protein binding pocket were taken from the recent X-ray crystallographic coordinates [1]. The three amino acids with potential cofactor interactions (Phe A689, Trp A697 and Leu A722) were explicitly considered in the calculations. In order to avoid artefacts from a too restricted model, peptide bonds to the next nearest amino acids (in the case of Phe A689, Leu A722) were also taken into account (see Fig. 8). The phytyl chain of the quinone was replaced by an ethyl group, which does not alter the electronic structure of the quinone moiety [34]. The model of the A_1 cofactor in the protein binding pocket consisting of 95 atoms was completely geometry-optimized imposing no constraints on the structure. Being aware of deficiencies of the DFT approach for geometry optimizations in noncovalently bonded systems, we have, because of the size of the problem, nevertheless used this method for optimizing the structure prior to calculations of the magnetic resonance parameters.

Comparison of the geometry-optimized model binding pocket of A_1 with the crystal structure shows good agreement. Thus, it can be safely assumed that the model pocket can be used for a structural description of the protein surrounding

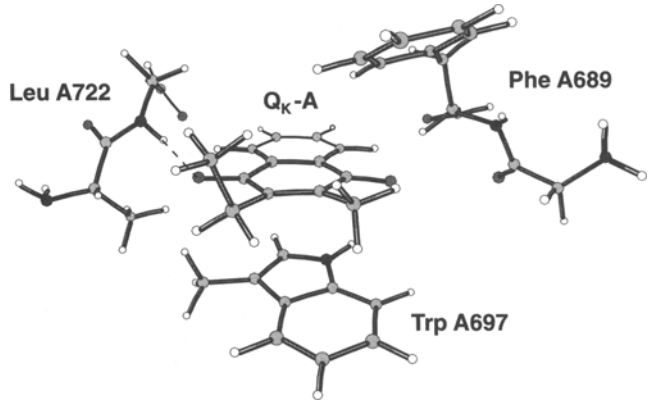

Fig. 8. Model of the A_1 binding site in the PsaA subunit [1] used for DFT calculations (see text). Carbon, grey; oxygen, dark grey; nitrogen, black; hydrogen, white. The dashed line indicates the H-bond between O-4 of the quinone and the backbone NH of Leu A722.

of A_1. The binding pocket of A_1 is based on the X-ray structure of the diamagnetic ground state. Upon formation of the radical anion $A_1^{-\bullet}$ larger interaction with the protein, i.e., stronger H-bonds and other dipolar interactions, are expected. Indeed, the distance of the H-bond to Leu A722 is shortened from 0.174 to 0.156 nm and Trp A697 is shifted towards the quinone, resulting in a smaller distance from N(Trp) to O-1 (Fig. 8).

From this geometry-optimized structure we obtained g-tensor principal values which are in reasonably good agreement with the experiment (see Table 4). Whereas for g_z and for g_y the differences between calculation and experiment are almost within experimental error (± 0.0001), we found a significant deviation for the g_x-value. It is known that DFT calculations of g-tensors of small organic radicals like phenoxyl [35] and quinone anion radicals [33] tend to overestimate Δg_x. In a recent work on quinone anion radicals [33] it was found that g_x deviates systematically by about $6 \cdot 10^{-4}$. This result was traced back to a deficiency of the chosen functional. This systematic error has to be taken into account in our calculations and could explain the deviation in g_x.

The effect of single amino acids can be rationalized by calculation of the g-tensor on the geometry-optimized model for $A_1^{-\bullet}$ including only the respective amino acid (Table 4). Each amino acid leads to a reduction of the g-anisotropy. The largest influence on Δg_x has Leu A722 that lowers the g_x-value by $11 \cdot 10^{-3}$, which is mainly attributed to the H-bond formation; next come Trp A697 ($\Delta g_x = -7 \cdot 10^{-4}$) and Phe A689 ($\Delta g_x = -4 \cdot 10^{-4}$). Addition of a second amino acid, with cyclic permutations of the amino acids nearly shows an additional effect on the g-values. Whereas the influence onto g_x is most significant, g_y is moderately reduced and g_z remains basically unchanged.

As an additional probe, the ^{1}H hfc of the 2-CH_3 group of the quinone and of the proton(s) in H-bonds can be used. The comparison with the experimental values shows that the increased CH_3 hfc in $A_1^{-\bullet}$ ($A_{iso}^{exp} = 10.3$ MHz) can indeed be reproduced ($A_{iso}^{calc} = 9.8$ MHz) and traced back to the strong single H-bond to O-4

Table 4. Calculated g-tensor principal values of $A_1^{-\bullet}$ as obtained from the geometry-optimized model (Fig. 8).

Model[a]	g_x	g_y	g_z
$VK_1^{-\bullet}$ naked	2.0099	2.0058	2.0021
$VK_1^{-\bullet}$ + Phe698	2.0095	2.0057	2.0021
$VK_1^{-\bullet}$ + Trp697	2.0092	2.0057	2.0020
$VK_1^{-\bullet}$ + Leu722	2.0088	2.0056	2.0020
$VK_1^{-\bullet}$ + Phe698 + Trp697	2.0088	2.0054	2.0021
$VK_1^{-\bullet}$ + Phe698 + Leu722	2.0082	2.0055	2.0020
$VK_1^{-\bullet}$ + Trp697 + Leu722	2.0081	2.0054	2.0020
$VK_1^{-\bullet}$ + Phe698 + Leu722 + Trp697	2.0075	2.0052	2.0020
$A_1^{-\bullet}$ (PS I)	2.0063	2.0051	2.0022

[a] The effect of the particular amino acids is investigated by removing the other amino acids from the geometry-optimized model.

of $A_1^{-\bullet}$ (which was also suggested earlier [34]). However, the placement of Trp A697 seems to present a problem in the calculations since it lowers the A_{CH_3} value (see ref. 36 for details). The calculated H-bond hf tensor [36] agrees quite well with that reported in ref. 5. In addition to these hfcs, the DFT calculations also show spin density delocalization from the quinone moiety onto surrounding amino acids (Leu A722 and Trp A697), leading to substantial spin density, e.g., at the nitrogen nuclei. Such effects were observed in electron spin echo envelope modulation experiments [37] but will not be further discussed here, see ref. 36.

3.5 Summary and Conclusion

It was shown that by application of high-field EPR spectroscopy the *g*-tensor of organic radicals exhibiting small *g*-anisotropy can be resolved. This was demonstrated here for $VK_1^{-\bullet}$ in organic solvents and $A_1^{-\bullet}$ in PS I with a multifrequency approach. In case of chlorophyll radicals the *g*-anisotropy is very small compared to the inhomogeneous linewidth and *g* is not resolved in powder spectra at W-band. The situation is improved when single crystals are used. This led to a determination of the *g*-tensor magnitude and orientation for $P_{700}^{+\bullet}$.

Particular emphasis was placed on the phylloquinone acceptor radical anion $A_1^{-\bullet}$ in PS I. This species exhibits unusually large *g*-tensor principal values which were found to be similar to those of $VK_1^{-\bullet}$ in an apolar, nonprotic solvent cage in our in vitro experiments. Obviously, this quinone is situated in a very hydrophobic protein surrounding. Inspection of the X-ray structure indeed shows only hydrophobic aliphatic and aromatic amino acids forming the binding pocket of A_1 (Fig. 8). Exchange experiments (C. Teutloff, unpubl.) show that H/D exchange is very difficult supporting the hydrophobic character of the protein pocket. The detected presence of a hydrogen bond to one of the carbonyl oxygens of A_1 leads to an asymmetry of the spin density distribution in the radical anion and affects the hyperfine couplings significantly. Such an H-bond should decrease the *g*-anisotropy. In spite of this effect, the detected *g*-values of $A_1^{-\bullet}$ are still very large showing the dominance of the hydrophobic amino acids (see Fig. 8). Density functional calculations performed on $VK_1^{-\bullet}$ in a surrounding modeled on the recent X-ray crystallographic structure indeed show a fairly large *g*-tensor in spite of the existence of a tight H-bond to a backbone NH of a leucine ([36] and this work). It can be assumed that the H-bond mainly has a structural function fixing the quinone in the correct position for optimum electron transfer.

The most remarkable feature of $A_1^{-\bullet}$ is its very negative midpoint potential E_m (approximately -750 to -810 mV [38, 39]) which is optimized for electron transfer in PS I from A_0 to F_x (Fig. 1). The E_m of VK_1 in polar protic solvents is much higher (-170 mV in water [40]). It is, however, interesting that in nonprotic solvents of lower polarity this value is more negative (approximately -570 mV in dimethyl formamide [41]). Even lower values can be expected for ethers.

It has been shown that the *g*-anisotropy is a good measure for the polarity of a radical's surrounding as known from other works [42–44]. The large *g*-anisot-

ropy observed for $A_1^{-\bullet}$ is therefore indicative for the apolar, hydrophobic binding pocket which is in line with the unusual midpoint potential and high reducing power of this quinone radical in PS I. Incorporation of plastoquinone-9 (PQ-9) instead of VK_1 in pathway mutants of *Synechocystis* strain PCC 6803 led to a similar shift of the midpoint potential. For plastoquinone-9 in the A_1 site of PS I an $E_m \approx -610$ mV was estimated [45], whereas for this quinone in water only -74 mV have been reported [40]. This shows that it is indeed the protein surrounding that determines the redox properties of this cofactor and not so much the type of the quinone present in the site. For a quantitative evaluation of the relationship between midpoint potential and magnetic resonance parameters like the *g*-tensor more experimental and theoretical work, regarding the redox potentials in different solvents, is required.

Acknowledgements

We thank P. Fromme (TU Berlin) for providing the PS I samples, N. Krauß and P. Jordan (FU Berlin) for information about the X-ray structure and D. Stehlik (FU Berlin) for helpful discussions. This work was supported by DFG (SPP 1051, Sfb 498, TP C2 and C5), Volkswagen-Stiftung, EU (FMRX-CT98-0214) and Fonds der Chemischen Industrie (to W.L.).

References

1. Jordan P., Fromme P., Witt H.T., Klukas O., Saenger W., Krauß N.: Nature **411**, 909 (2001)
2. Webber A.N., Lubitz W.: Biochim. Biophys. Acta **1507**, 61 (2001)
3. Diner B.A., Babcock G.T. in: Oxygenic Photosynthesis: The Light Reactions (Ort D.R., Yocum C.F., Heichel I.F., eds.), pp. 213–247. Dordrecht: Kluwer Academic Publishers 1996.
4. van der Est A., Prisner T., Bittl R., Fromme P., Lubitz W., Möbius K., Stehlik D.: J. Phys. Chem. **101**, 1437 (1997)
5. Rigby S., Evans M.C.W., Heathcote P.: Biochemistry **35**, 6651 (1996)
6. Teutloff C., MacMillan F., Bittl R., Lendzian F., Lubitz W. in: Photosynthesis: Mechanisms and Effects (Garab G., ed.), vol. I, pp. 607–610. Dordrecht: Kluwer Academic Publishers 1998.
7. Bratt P.J., Poluektov O.G., Thurnauer M.C., Krzystek J., Brunel L.C., Schrier J., Hsiao Y.W., Zerner M., Angerhofer A.: J. Phys. Chem. B **104**, 6973 (2000)
8. Hales B.J., Case E.E.: Biochim. Biophys. Acta **637**, 291 (1981)
9. Burghaus O., Plato M., Rohrer M., Möbius K., MacMillan F., Lubitz W.: J. Phys. Chem. **97**, 7639 (1993)
10. MacMillan F., Hanley J., van der Weerd L., Knüpling M., Un S., Rutherford A.W.: Biochemistry **36**, 9297 (1997)
11. Teutloff C., MacMillan F., Bittl R., Lendzian F., Lubitz W. in: Magnetic Resonance and Related Phenomena (Ziessow D., Lubitz W., Lendzian F., eds.), vol. II, pp. 806–807. Berlin: Technische Universität Berlin 1998.
12. Stehlik D., Möbius K.: Annu. Rev. Phys. Chem. **48**, 745 (1997)
13. van der Est A.: Biochim. Biophys. Acta **1507**, 212 (2001)
14. Bittl R., Zech S.: Biochim. Biophys. Acta **1507**, 194 (2001)
15. Stesmans A., van Gorp G.: Rev. Sci. Instrum. **60**, 2949 (1989)
16. Fromme P., Witt H.T.: Biochim. Biophys. Acta **1365**, 175 (1998)
17. Zech S.G., Hofbauer W., Kamlowski A., Fromme P., Stehlik D., Lubitz W., Bittl R.: J. Phys. Chem. B **104**, 9728 (2000)

18. Nimz O., Lendzian F., Boullais C., Lubitz W.: Appl. Magn. Reson. **14**, 255 (1998)
19. DGauss 4.0. Cray Research Inc., San Diego 1995.
20. Scientific Computing and Modelling NV: ADF Program System, Release 2000.02. Vrije Universiteitar; Theoretical Chemistry, De Boelelaan 1083, 1081 HV Amsterdam, The Netherlands (2000)
21. Frisch M.J., Trucks G.W., Schlegel H.B., Robb G.E.S.M.A., Cheesemancw J.R., Zakrzewski V.G., Montgomery J.A.Jr., Stratmann R.E., Burant J.C., Dapprich S., Millam J.M., Daniels A.D., Kudin K.N., Strain M.C., O. Farkas J.T., Barone V., Cossi M., Cammi R., Mennucci B., Pomelli C., Adamo C., Clifford S., Ochterski J., Petersson G.A., Ayala P.Y., Cui Q., Morokuma K., Malick D.K., Rabuck A.D., Raghavachari K., Foresman J.B., Cioslowski J., Ortiz J.V., Baboul A.G., Stefanov B.B., Liu G., Liashenko A., Piskorz P., Komaromi I., Gomperts R., Martin R.L., Fox D.J., Keith T., Al-Laham M.A., Peng C.Y., Nanayakkara A., Gonzalez C., Challacombe M., Gill P.M.W., Johnson B.G., Chen W., Wong M.W., Andres J.L., Head-Gordon M., Replogle E.S., Pople J.A.: Gaussian98, Revision A.6 Tech. Rep. Gaussian, Inc., Pittsburgh PA 1998.
22. Prisner T.F., McDermott A.E., Un S., Norris J.R., Thurnauer M.C., Griffin R.G.: Proc. Natl. Acad. Sci. USA **90**, 9485 (1993)
23. Bratt P.J., Rohrer M., Krzystek J., Evans M.C.W., Brunel L.C., Angerhofer A.: J. Phys. Chem. B **101**, 9686 (1997)
24. Käss H., Fromme P., Witt H.T., Lubitz W.: J. Phys. Chem. B **105**, 1225 (2001)
25. Krabben L., Schlodder E., Jordan R., Carbonera D., Giacometti G., Lee H., Webber A.N., Lubitz W.: Biochemistry **39**, 13012 (2000)
26. Boudreaux B., MacMillan F., Teutloff C., Agalarov R., Gu F., Grimaldi S., Bittl R., Brettel K., Redding K.: J. Biol. Chem. **276**, 37229 (2001)
27. Link G., Bechthold T., Bechthold M., Weidner J.-U., Ohmes E., Tang J., Poluektov O., Utschig L., Schlesselmann S.L., Thurnauer M.C., Kothe G.: J. Am. Chem. Soc. **123**, 4211 (2001)
28. Klette R., Törring J., Plato M., Möbius K., Bönigk B., Lubitz W.: J. Phys. Chem. **97**, 2015 (1993)
29. Prisner T.F., van der Est A., Bittl R., Lubitz W., Stehlik D., Möbius K.: Chem. Phys. **194**, 361 (1995)
30. Stone A.J.: Proc. R. Soc. Lond. A **271**, 424 (1963)
31. Lubitz W., Feher G.: Appl. Magn. Reson. **17**, 1 (1999)
32. Knüpling M., Törring J.T., Un S.: Chem. Phys. **219**, 291 (1997)
33. Kaupp M., Remenyi C., Vaara J., Malkina O.L., Malkin V.G.: J. Am. Chem. Soc. (2001) in press.
34. O'Malley P.J.: Biochim. Biophys. Acta **1411**, 101 (1999)
35. Malkina O.L., Vaara J., Schimmelpfennig B., Munzarová M., Malkin V.G., Kaupp M.: J. Am. Chem. Soc. **122**, 9206 (2000)
36. Teutloff C., Bittl R., Stein M., Jordan P., Fromme P., Krauß N., Lubitz W. in: PS2001 Proceedings – 12th International Congress on Photosynthesis. Melbourne: CSIRO Publishing (2001)
37. Hanley J., Deligiannakis Y., MacMillan F., Bottin H., Rutherford A.W.: Biochemistry **36**, 11543 (1997)
38. Iwako M., Itoh S.: Plant Cell Physiol. **35**, 983 (1994)
39. Setif P., Bottin H., Brettel K. in: Current Research in Photosynthesis (Baltscheffsky M., ed.), vol. 2, pp. 539–546. Dordrecht: Kluwer Academic 1990.
40. Swallow A.J. in: Function of Quinones in Energy Conserving Systems (Trumpower B.L., ed.), pp. 59–72. New York: Academic Press 1982.
41. Schmid R., Goebel F., Warnecke A., Labahn A.: J. Chem. Soc. Perkin Trans. **2**, 1199 (1999)
42. Kawamura T., Matsunami S., Yonezawa T.: Bull. Chem. Soc. Jpn. **40**, 1111 (1967)
43. Ondar M.A., Grinberg O.Y., Doubinskii A.A., Lebedev Y.S.: Sov. J. Phys. Chem. **3**, 781 (1985)
44. Steinhoff H.J., Savitsky A., Wegener C., Pfeiffer M., Plato M., Möbius K.: Biochim. Biophys. Acta **1457**, 253 (2000)
45. Semenov A.Y., Vassiliev I.L., van der Est A., Zybailov M.D.M.B., Shen G., Stehlik D., Diner B.A., Chitnis P.R., Golbeck J.H.: J. Biol. Chem. **275**, 23429 (2000)

Authors' address: Wolfgang Lubitz, Max-Planck-Institut für Strahlenchemie, Stiflstrasse 34-36, 45470 Mülheim an der Ruhr, Germany